# Wind-Forced Variability of the Zonal Overturning Circulation

MICHAEL A. SPALL<sup>a</sup>

<sup>a</sup> Woods Hole Oceanographic Institution, Woods Hole, Massachusetts

(Manuscript received 11 August 2021, in final form 21 December 2021)

ABSTRACT: The mechanisms of wind-forced variability of the zonal overturning circulation (ZOC) are explored using an idealized shallow water numerical model, quasigeostrophic theory, and simple analytic conceptual models. Two wind-forcing scenarios are considered: midlatitude variability in the subtropical/subpolar gyres and large-scale variability spanning the equator. It is shown that the midlatitude ZOC exchanges water with the western boundary current and attains maximum amplitude on the same order of magnitude as the Ekman transport at a forcing period close to the basin-crossing time scale for baroclinic Rossby waves. Near the equator, large-scale wind variations force a ZOC that increases in amplitude with decreasing forcing period such that wind stress variability on annual time scales forces a ZOC of O(50) Sv  $(1 \text{ Sv} \equiv 10^6 \text{ m}^3 \text{ s}^{-1})$ . For both midlatitude and low-latitude variability the ZOC and its related heat transport are comparable to those of the meridional overturning circulation. The underlying physics of the ZOC relies on the influences of the variation of the Coriolis parameter with latitude on both the geostrophic flow and the baroclinic Rossby wave phase speed as the fluid adjusts to time-varying winds.

SIGNIFICANCE STATEMENT: The purpose of this study is to better understand how large-scale winds at mid- and low latitudes move water eastward or westward, even in the deep ocean that is not in direct contact with the atmosphere. This is important because these currents can shift where heat is stored in the ocean and if it might be released into the atmosphere. It is shown that large-scale winds can drive rapid cross-basin transports of water masses, especially so at low latitudes. The present results provide a guide on what controls this motion and highlight the importance of large-scale ocean waves on the water movement and heat storage.

KEYWORDS: Ekman pumping/transport; Mass fluxes/transport; Planetary waves; Rossby waves

# 1. Introduction

The oceanic thermohaline overturning circulation refers to a redistribution of mass, heat, and salt, sometimes framed in depth coordinates and sometimes framed in density coordinates. Fluxes of properties across density surfaces require some form of turbulent mixing, while fluxes along density surfaces can take place in the absence of mixing. This movement of water masses is important for the climate system because it can redistribute heat, salt, and other tracers thousands of kilometers across the ocean basins and alter air–sea fluxes and net exchanges with the atmosphere. These overturning circulations are inherently three-dimensional in nature, involving zonal, meridional, and vertical displacements.

Theoretical, observational, and modeling studies have largely been focused on the zonal average of the overturning circulation, which projects this three-dimensional process onto two dimensions, latitude and depth. This so-called meridional overturning circulation (MOC) is of great interest because it transports as much as 1.25 PW of heat poleward (McCarthy et al. 2015; Roemmich and Wunsch 1985), significantly influencing both climate and weather. This meridional heat transport connects the heat loss at high latitudes with the heat gain at low latitudes (and at southern high latitudes in the Atlantic Ocean). However, the mean surface heat flux also has a systematic pattern in the zonal direction with most

of the heat loss taking place over the western boundary currents and most of the heat gain taking place in the eastern subtropical basins or equatorial regions. Taking the meridional average of the zonal transports produces a circulation in the longitude/depth plane called the zonal overturning circulation (ZOC). This characterization of the circulation has received little attention to date. However, as pointed out by Wei et al. (2015), the mean zonal heat flux in the central Pacific Ocean exceeds 1 PW and in the Atlantic it is close to 0.5 PW. These are comparable to the meridional heat flux carried by the meridional overturning circulation.

The oceans have taken up over 90% of the global heat gain over the past 60 years (Levitus et al. 2012; Abraham et al. 2013). This heat storage and exchange with the atmosphere varies strongly on seasonal to interannual and decadal time scales. Model studies indicate that wind-forcing is important for much of this observed variability in heat content at both mid- and low latitudes (Lozier et al. 2008; Grist et al. 2010; Häkkinen et al. 2015; Williams et al. 2014; Evans et al. 2017; Pillar et al. 2016; Tandon et al. 2020). Huang (2015) termed such adiabatic, wind-driven oscillations of heat content as heaving modes.

The nonlocal response to low-frequency wind anomalies represents an important element of the global meridional overturning circulation and heat and freshwater storage. This was demonstrated in numerous studies using idealized numerical models, realistic global models, and theory. Cessi and Otheguy (2003) found that oscillating winds in one basin could excite a strong remote response in other basins, with

Corresponding author: Michael A. Spall, mspall@whoi.edu

DOI: 10.1175/JPO-D-21-0174.1

information communicated by baroclinic boundary and interior Rossby waves. The boundary waves rapidly equilibrate the pressure on the eastern boundary, which then radiates westward as baroclinic Rossby waves with distortions resulting from the meridional dependence of the phase speed. Similar cross-hemisphere communication and Rossby wave radiation was found for localized buoyancy forcing by Kawase (1987). Cessi et al. (2004) found a similar response in a realistically configured global climate model. Johnson and Marshall (2004) developed a theory for global telecommunications forced by transport anomalies at high latitudes in a single basin and found that the equator can act as a low-pass filter to MOC anomalies' ability to cross into the other hemisphere. These studies demonstrate the importance of wind forcing for isopycnal heaving and heat storage and the role of boundary and Rossby waves in mediating the response.

Simple wind-driven models are also able to reproduce much of the observed seasonal to interannual variability in the MOC as measured by the RAPID/MOCHA array at 26.5°N in the North Atlantic (Kanzow et al. 2010; Zhao and Johns 2014a,b; Yang 2015; Pillar et al. 2016; Zou et al. 2019, 2020). Sturges and Hong (1995) found similar good agreement using a simple wind-forced, linear, reduced gravity model for the low-frequency variability of sea surface height at Bermuda. Several recent studies using more complete basin and global scale models have found wind forcing to be dominant at interannual and shorter time scales and buoyancy forcing to be most important for decadal MOC variability (Biastoch et al. 2008; Yeager and Danabasoglu 2014; Polo et al. 2014; Pillar et al. 2016). On interannual time scales, Grist et al. (2010) found that changes in ocean heat content in the North Atlantic were dominated by advective flux convergence, not air-sea exchange. Tandon et al. (2020) have found that the meridional heat transport in the Pacific Ocean forced by winds on annual to interannual time scales is the dominant component of the interannual variability in global meridional heat transport.

These previous studies indicate that winds are the dominant forcing mechanism for variability in regional ocean heat content on annual to interannual time scales. This has been primarily diagnosed in terms of variability in the MOC and the related meridional transport of heat. However, as demonstrated by Huang (2015) and Wei et al. (2015), winds can also force variability in the ZOC and shift heat storage zonally. The dynamics of the variability in the ZOC, however, are much less well understood. The objective of the present study is to identify the mechanisms governing variability in the ZOC and its sensitivity to the forcing frequency and environmental parameters. Two patterns of wind variability are chosen: midlatitude gyre strength and large-scale, crossequatorial zonal winds. The former represents the dominant mode of wind variability and interannual time scales (Zou et al. 2020). The large-scale wind pattern was chosen to illustrate the controlling dynamics at low latitudes, where more realistic models find very large wind-driven fluctuations in the MOC and ZOC (Blaker et al. 2021; Bell et al. 2021). The understanding gained from these idealized configurations

should remain relevant to other, more complex, forcing scenarios.

## 2. A two-layer shallow water model

Examples of zonal overturning forced by periodic winds are provided by a two-layer shallow water numerical model on an equatorial beta plane. The model solves the momentum and continuity equations on a staggered horizontal *C* grid.

The horizontal momentum equations can be written for two isopycnal layers as

$$D_{t}\mathbf{u}_{1} + \mathbf{f} \times \mathbf{u}_{1} = \frac{\tau}{\rho_{0}h_{1}} - g\nabla(h_{1} + h_{2}) + A\nabla^{2}\mathbf{u}_{1},$$

$$D_{t}\mathbf{u}_{2} + \mathbf{f} \times \mathbf{u}_{2} = -g\nabla(h_{1} + h_{2}) + g'\nabla h_{1} + A\nabla^{2}\mathbf{u}_{2}, \quad (1)$$

where

$$D_t = \frac{\partial}{\partial t} + \mathbf{u} \cdot \nabla, \ g' = (\rho_2 - \rho_1)g/\rho_2, \tag{2}$$

where  $\rho_0$  is a reference density, and  $\mathbf{u}_i$  and  $h_i$  are the horizontal velocity vectors and layer thicknesses for layer *i*. The wind stress vector is purely zonal, i.e.,  $\boldsymbol{\tau} = (\tau^x, 0)$ . The constant Laplacian viscosity with coefficient A is used for momentum dissipation.

The continuity equation, with no diapycnal mixing between layers, is

$$\frac{\partial h_k}{\partial t} + \nabla \cdot (h_k \mathbf{u}_k) = A_h \nabla^2 h_k. \tag{3}$$

There is a horizontal diffusion of layer thickness with coefficient  $A_h$ .

The Coriolis parameter varies linearly with y as  $\mathbf{f} = \beta y\mathbf{z}$ , where  $\beta = 2 \times 10^{-11} \text{ m}^{-1} \text{ s}^{-1}$ . The initial layer thicknesses are  $h_1 = 1000 \text{ m}$  and  $h_2 = 3000 \text{ m}$ , and the reduced gravity between the two layers is  $g' = 0.01 \text{ kg m}^{-3}$ . This gives a baroclinic deformation radius of 39 km and a baroclinic Rossby wave speed of 3 cm s<sup>-1</sup> at y = 3500 km.

The model is configured in a rectangular domain that is  $L=6000~\rm km$  in zonal extent and 12000 km in meridional extent. The equator is located at the meridional midpoint, so the model domain spans -L < y < L. The grid spacing is 40 km with lateral viscosities of  $A=A_h=500~\rm m^2~s^{-1}$ . At this resolution and viscosity the model is not eddy resolving, although instabilities do emerge for some parameter choices. The side boundary conditions are no-slip and no normal flow.

The purpose of these model calculations is to demonstrate the basic, large-scale response to time variable winds and how it depends on the forcing frequency and model parameters. The numerical model also provides a more dynamically complete basis for evaluating the simple quasigeostrophic theory developed in the following section. As such, the mean circulation is ignored and the variability in circulation and isopycnal thicknesses resulting from idealized, periodic perturbations in surface winds is explored. Spall (2021) found that the mean circulation representative of the subtropical and subpolar gyres did not alter the variability forced by similar wind anomalies, even for strongly nonlinear flows.

The model will be forced with two types of periodic wind anomalies with frequency  $\omega=2\pi/P$ . The first is centered at midlatitudes and represents a strengthening/weakening of the subtropical and subpolar gyres. This was found to be the dominant mode of variability at interannual frequencies by Zou et al. (2020). The gyre boundary is located at  $y=y_0$  and the gyres have a meridional extent of  $L_g$ . The wind stress is zero outside the latitude range of the two gyres:

$$\tau(y, t) = \frac{1}{2} \tau_0 [1 + \cos \pi (y - y_0) / L_g] \sin \omega t, \quad y_0 - L_g < y < y_0 + L_g,$$

$$\tau = 0, \qquad |y - y_0| \ge L_g.$$
(4)

The second type of wind forcing represents large-scale variability in the zonal wind stress. The cleanest way to achieve this is by applying a simple spatially uniform zonal wind that oscillates in time. As will be shown below, this emphasizes the dynamics at low latitudes, where more realistic models have found very large wind-driven fluctuations in the meridional overturning circulation at synoptic to annual time scales. Although the large-scale wind pattern used here is not very realistic, it has the advantages of not introducing abrupt wind stress curl patterns and has no inherent length scale. This simplicity will prove useful in identifying the processes and internal dynamics controlling the ZOC at low latitudes:

$$\tau(t) = \tau_0 \sin \omega t. \tag{5}$$

Each of these wind stress patterns results in Ekman pumping, which forces both horizontal and vertical transports and drives both a ZOC and an MOC. The Ekman pumping rate is given by its meridional structure  $W_E(y)$  modulated by a periodic oscillation  $\sin \omega t$ . For the gyre pattern the Ekman pumping is dominated by the variation of wind stress with latitude. This approximation neglects the variation of the Coriolis parameter with latitude, which is  $O(L_{\phi}/\pi y)$  smaller than (6):

$$W_E(y) = \frac{\pi \tau_0}{\rho_0 \beta y L_g} \sin \left[ \frac{\pi (y - y_0)}{L_g} \right]. \tag{6}$$

For the large-scale oscillating winds, the Ekman pumping arises as a result of the variation in the Coriolis parameter with latitude:

$$W_E(y) = -\frac{\tau_0}{\rho_0 \beta y^2}. (7)$$

Note that the Ekman pumping in this case gets very large as the equator is approached and that the Ekman pumping is symmetric about the equator.

## a. Midlatitude gyre variability

An example of the circulation anomalies forced by oscillations in the strength of midlatitude subtropical and subpolar gyres is provided by wind forcing (4) with  $\tau_0 = 0.05$  N m<sup>-2</sup>,  $y_0 = 2500$  km,  $L_g = 2000$  km, and P = 10 years. This produces a maximum Ekman transport at the gyre boundary of  $4.2 \times 10^6$  m<sup>3</sup> s<sup>-1</sup>. The time for a first mode baroclinic Rossby wave to cross the basin at the latitude of the gyre boundary is about

6.5 years. At this forcing period waves have fully crossed the basin in the subtropical gyre over a forcing period while those at the northern limit of the subpolar gyre will not yet have crossed the basin. The thickness of the upper layer after 20 years of integration (two forcing periods) is shown in Fig. 1a. The wind stress is transitioning from a negative anomaly to a positive anomaly, so the 5 years prior to this time the Ekman pumping in the subtropical gyre was upward. This is reflected in the relatively thin upper layer in the western subtropical gyre. There is a similarly weak subpolar gyre indicated by the positive layer thickness anomaly. Because Rossby waves propagate more slowly at higher latitudes, this signal is still found in the middle of the basin. The time rate of change of the upper layer thickness (Fig. 1b) shows that these layer thickness anomalies are propagating westward. However, these signals do not simply originate at the eastern boundary and propagate westward, as in Anderson and Gill (1975), because they are forced all across the basin as they propagate. This results in a wave speed that is twice the unforced long Rossby wave propagation speed (White 1977; LaCasce 2000; Spall 2021). Cessi and Otheguy (2003) and Johnson and Marshall (2004) tie this latitudinal dependence of the Rossby wave phase speed to the global mass balance through the equilibration of boundary pressure via low-frequency waves.

This is evident in panels Figs. 1c and 1d, which show the upper layer thickness as a function of time and longitude at the midlatitude of the subtropical (Fig. 1c) and subpolar (Fig. 1d) gyres. The phase propagation in the subtropical gyre is faster than that in the subpolar gyre. The maximum signal is found on the western boundary within the subtropical gyre while that in the subpolar gyre is found in the middle of the basin. This is because the Ekman pumping changes sign before the wave can cross the basin in the subpolar gyre. The phase speed is close to 2 times the first mode baroclinic Rossby wave speed (green dashed lines) and much faster than that expected for a free wave (green solid lines), as expected from the quasigeostrophic theory of White (1977).

The zonal overturning circulation  $\Psi_Z$  calculated over the final 10-yr period of the 20-yr integration is shown in Fig. 2a. The overturning is calculated by integrating the zonal transport in the upper layer from the eastern boundary to the western boundary over the entire meridional extent of the domain:

$$\Psi_{Z}(x,t) = \int_{L}^{x} \int_{L}^{L} u_{1} h_{1} \, dy \, dx. \tag{8}$$

Because there is no diapycnal mixing in the model, this represents a reorganization of mass within each density layer. Since the surface is very rigid, there is an essentially equal and opposite transport in the second layer. The overturning has a maximum amplitude of 1.9 Sv (1 Sv  $\equiv$  10<sup>6</sup> m<sup>3</sup> s<sup>-1</sup>) with a phase that is a function of longitude. The amplitude of the fluctuation in Ekman transport at the gyre boundary is 4.2 Sv, so the ZOC represents approximately 50% of this meridional transport. The oscillation is a maximum on the western boundary and monotonically decreases toward zero at the eastern boundary. The ZOC exchanges water between the

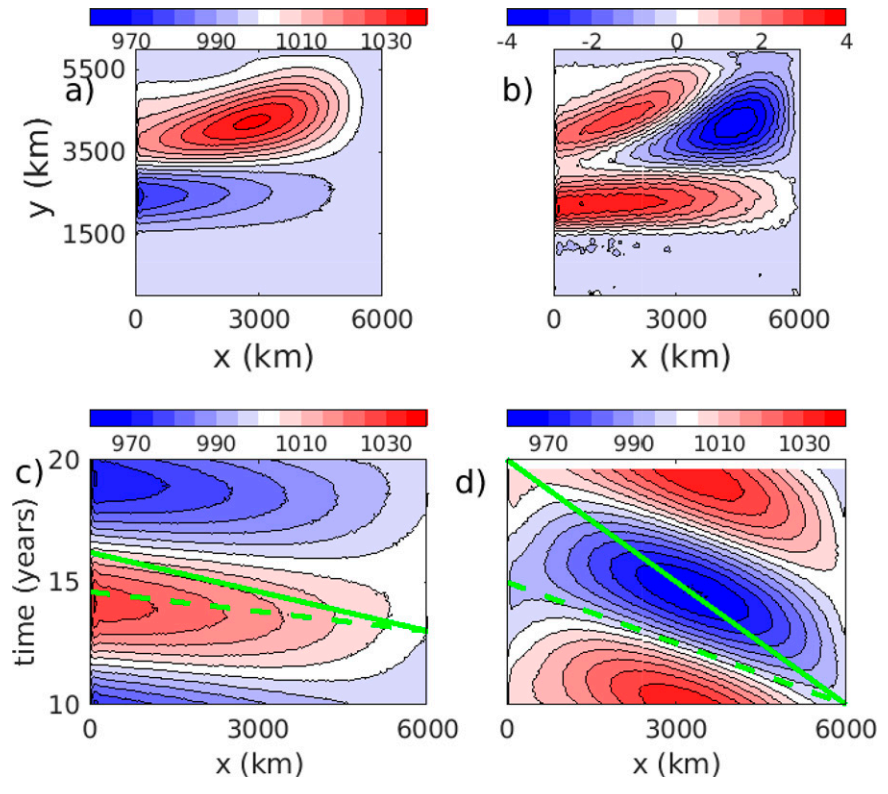


FIG. 1. (a) Upper layer thickness (m) and (b) time rate of change of upper layer thickness  $(10^{-7} \text{ m s}^{-1})$  for the shallow water model after 20 years of integration with midlatitude gyre variability in the winds (4) and a 10-yr period. The layer thickness as a function of longitude and time at (c) y = 2500 km (subtropical gyre) and (d) y = 4500 km (subpolar gyre). The solid green lines indicate the first mode baroclinic Rossby wave speed  $c_1$  while the dashed green lines are  $2c_1$ .

western boundary current and the basin interior, pulling water off the boundary for negative wind anomalies and returning water toward the boundary during positive wind anomalies. The maximum meridional overturning circulation for this calculation is of similar magnitude (3.2 Sv) and is centered on the gyre boundary, where the maximum Ekman transport is located (Fig. 1b). The MOC is not symmetric in latitude,

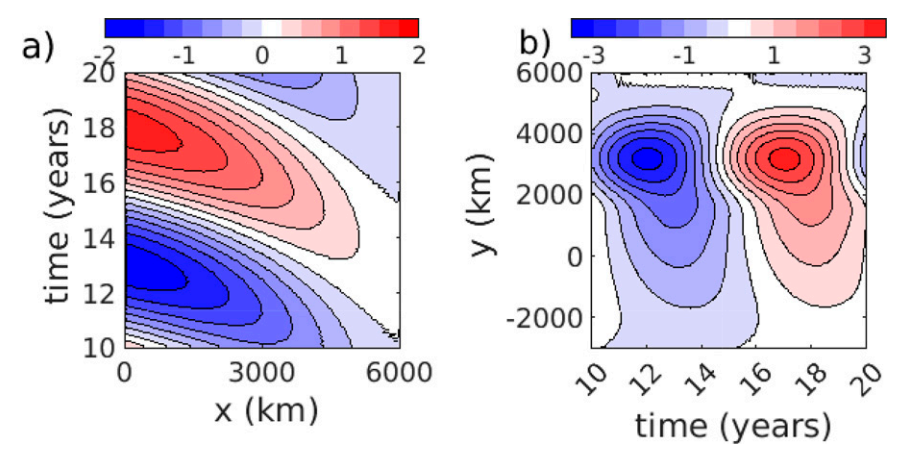


FIG. 2. (a) The zonal overturning circulation (Sv) and (b) the meridional overturning circulation (Sv) for the shallow water model with midlatitude gyre variability in the winds (4) and a 10-yr period.

however, as it extends southward beyond the latitude range of the variable wind stress and even crosses the equator. This is the remote MOC forced by a mass imbalance of the oscillating subtropical and subpolar gyres (Cessi and Otheguy 2003; Spall and Nieves 2020). This arises because the upper layer thickness in the subpolar gyre fluctuates more over a forcing period than does the upper layer thickness in the subtropical gyre. This is because the Coriolis parameter is smaller at lower latitudes and the gyre adjusts to surface forcing more quickly. As a result, the subpolar gyre stores or discharges more water than can be absorbed by the subtropical gyre. This fluid is either expelled to or supplied by western boundary currents that extend to low latitudes via Kelvin wave propagation. It is this same mass imbalance that gives rise to the ZOC at midlatitudes forced by the oscillating winds. It also is a clear demonstration that the overturning circulation is three-dimensional and that the MOC and ZOC can be strongly connected.

In a quasigeostrophic system in which  $f=f_0$  and is constant in latitude, the Ekman pumping in this case is antisymmetric about  $y=y_0$ . The interface displacement in the subtropical gyre is exactly balanced by the interface displacement in the subpolar gyre. Since the Coriolis parameter is constant, the deformation radius is uniform over the domain and the long Rossby wave phase speed is constant at  $c_1=\beta L_d^2$ . This results in a purely meridional overturning circulation in which the deepening of one gyre is exactly balanced by the shoaling of the other gyre. The mass flux required to deepen or shoal the thermocline is provided by a meridional overturning circulation (Spall 2021) and the ZOC vanishes.

However, if the Coriolis parameter increases with latitude, the baroclinic deformation radius decreases with latitude. The long Rossby wave speed decreases as  $f^{-2}$ , so that the subtropical gyre will adjust more quickly to changing winds than does the subpolar gyre. This means that the mass import/export required to balance the changing Ekman pumping in the subpolar gyre cannot be provided by the subtropical gyre and must come from the western boundary (Spall and Nieves 2020). When integrated over the interior of both the subtropical and subpolar gyres, the upper layer is either gaining or losing mass. The opposite is found for the lower layer. This is the mechanism by which time-varying midlatitude winds force both a zonal overturning circulation and a remote (lower latitude) meridional overturning circulation.

## b. Basin-scale variability

The second example considered is the periodic oscillation of large-scale winds, represented here by spatially uniform winds (5). In this case,  $\tau_0 = 0.05 \text{ N m}^{-2}$  and P = 5 years. The upper layer thickness at year 15 is shown in Fig. 3a. At this time the wind stress anomaly is zero but increasing from negative to positive. At low latitudes the layer thickness is nearly uniform across the basin while at higher latitudes we find increasingly shorter zonal wavelengths. The layer thickness is nearly uniform on the eastern boundary. The largest amplitude perturbations are located at midlatitudes. The time rate of change of the upper layer thickness is shown in Fig. 3b.

Near the equator the layer thickness is increasing near the eastern boundary and decreasing near the western boundary. This indicates a zonal flux of mass from west to east. At midlatitudes there is an alternating pattern of increasing and decreasing layer thickness that is shifted westward by one quarter wavelength from the layer thickness pattern. This is the signal of westward propagation of the thickness anomalies.

Unlike for the midlatitude case, the layer thickness on the eastern boundary varies with the wind stress (Fig. 4). The layer thickness oscillates nearly in phase with the wind with an amplitude of approximately 15 m. There is a slight phase lag at higher latitudes, but the layer thickness is nearly constant on the eastern boundary. This thickness variation on the eastern boundary provides a boundary condition for the analytic model in the following section. Its amplitude is set by the geostrophic flow that balances the Ekman pumping, as discussed further in section 4b.

The influence of this thickness anomaly on the eastern boundary is evident in the westward propagation of layer thickness depicted in Figs. 3c,d. The westward phase speeds at y = 2000 km and y = 4500 km show two distinct regions. The thickness anomaly on the eastern boundary shown in Fig. 4 can be seen propagating westward and decaying in time. There are also second thickness anomalies that emerge in midbasin. These take a maximum value on the western boundary at y = 2000 km and within the basin at y = 4500 km. These are the modes forced by the surface Ekman pumping. The signals propagating off the eastern boundary propagate slower, close to  $c_1$ , than the forced signals near the western boundary. This is consistent with White (1977). The distinction is more difficult to see at y = 4500 km because the forced signal is of weaker amplitude and propagates more slowly.

The ZOC for this case has a maximum amplitude of 3.7 Sv (Fig. 5a). It is now located near the midlongitude of the basin and the exchange with the western boundary is weak. There is a small phase shift such that the maximum overturning is found just before the maximum wind stress. The MOC (maximum value 1.4 Sv) is weaker than the ZOC and is located at about 2000-km latitude. The sense of the MOC is enhanced equatorward flow while the zonal wind stress is increasing. The MOC at mid- and high latitudes is weak because the Ekman pumping decreases with increasing latitude.

### 3. Quasigeostrophic theory

A simple analytic solution for a periodically forced quasigeostrophic ocean is used to aid in the interpretation of the shallow water model results. In particular, the theory demonstrates that the essential response is driven by information propagating from east to west and that the western boundary is essentially passive to the ZOC. The theory also identifies how the amplitude of the response depends on such things as the forcing frequency, stratification, the Coriolis parameter, and the Ekman pumping pattern.

The approach is similar to the 1.5 layer model of White (1977) but takes into account any number of vertical baroclinic modes, as in LaCasce (2000) and Spall (2021). The

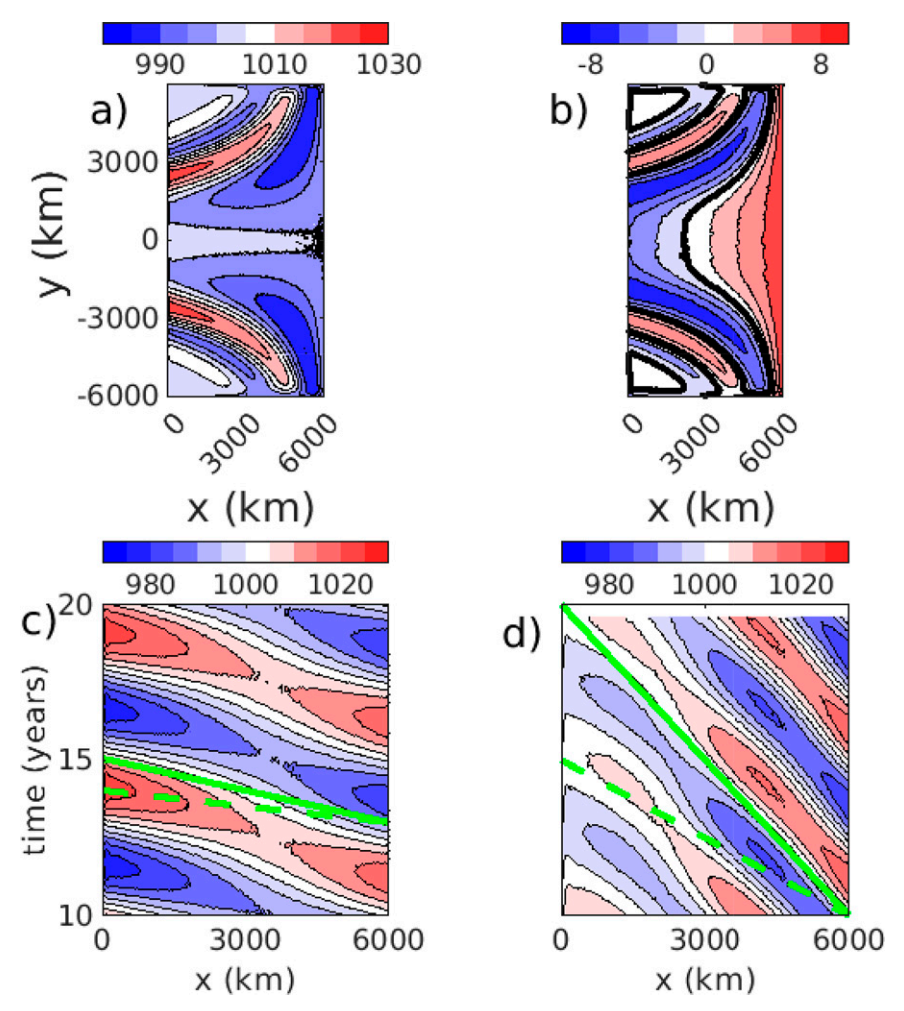


Fig. 3. (a) Upper layer thickness (m) and (b) time rate of change of upper layer thickness  $(10^{-7} \text{ m s}^{-1})$  for the shallow water model after 15 years of integration with basin-scale variability in the winds (5) and a 5-yr period. The layer thickness as a function of longitude and time at (c) y = 2000 km and (d) y = 4500 km. The solid green lines indicate the first mode baroclinic Rossby wave speed  $c_1$  while the dashed green lines are  $2c_1$ .

analytic model solves the linear, time-dependent, inviscid quasigeostrophic potential vorticity equation on a beta plane:

$$\frac{f_0^2}{N^2} \, \psi_{zzt} + \beta \psi_x = 0. \tag{9}$$

The Coriolis parameter is  $f_0$ ,  $N = (g/\rho_0 d\rho/dz)^{1/2}$  is the Brunt-Väisälä frequency,  $\beta$  is the meridional variation of the Coriolis parameter, and  $\psi$  is the velocity streamfunction. Subscripts z, x, and t indicate partial differentiation. The long wave approximation is made so that relative vorticity is neglected.

The model is forced by a periodic Ekman pumping at the surface that is independent of longitude and varies with latitude with magnitude  $W_E$  and frequency  $\omega$ . This provides a boundary condition for the streamfunction at the surface:

$$\psi_{zt} = \frac{N^2}{f_0} W_E(y) \sin \omega t, \quad z = 0.$$
 (10)

The standard quasigeostrophic equations assume that the Coriolis parameter in (9) and (10) are constant. As a result, the zonal phase speed of long Rossby waves is independent of latitude. However, because the long wave approximation is made, the governing equation (9) is independent of y. The solution to (9) will be applied over a range of latitudes with the Coriolis parameter set to its value at each latitude. An equatorial beta plane is used, so that  $f_0 = \beta y$ . Taking y as a parameter of the system allows the deformation radius, and thus the long Rossby wave speed, to vary with latitude.

Solutions for the streamfunction are sought that are wavelike in the zonal direction with wavelength  $2\pi/\lambda_n$ , frequency  $\omega$ , and vertical structure  $\phi$ :

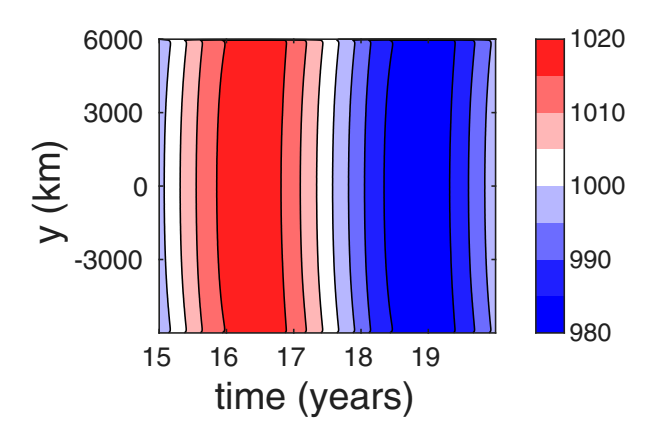


FIG. 4. Upper layer thickness (m) on the eastern boundary as a function of latitude and time for the shallow water model with basin-scale variability in the winds (5) and a 5-yr period.

$$\psi_n = \exp[i(\lambda_n x - \omega t)]\phi_n(z). \tag{11}$$

For simplicity, the stratification is taken to be uniform so that, from (9),  $\phi_n = 2^{1/2} \cos(n\pi z/D)$ , where *n* refers to the vertical mode, *D* is the bottom depth, and the scale factor of  $2^{1/2}$  is chosen to simplify the solution for  $\psi_n$ . The total solution is the sum of  $\psi_n$  over all modes.

The dispersion relation provides the zonal wavenumber for each vertical mode as a function of frequency:

$$\lambda_n = -\omega/(\beta L_n^2), \quad L_n = ND/(n\pi f_0), \tag{12}$$

where  $L_n$  is the baroclinic deformation radius for mode n.

It is assumed that there is no flow through the eastern boundary, so  $\psi$  is constant at x=0. The analytic model domain extends from x=0 at the eastern boundary to x=-L at the western limit of the domain. There is no boundary on the west, waves are simply allowed to propagate westward. The density anomaly on the eastern boundary,  $\psi_z$ , can vary in time with frequency  $\omega$ :

$$\psi_{zt} = \frac{N^2}{f} h'_n \sin(n\pi z/D) \cos\omega t, \quad x = 0.$$
 (13)

The eastern boundary condition is set by specifying  $h'_n$ , the maximum displacement of the density interface on the eastern boundary for mode n.

Multiplying the potential vorticity Eq. (9) by  $\phi_n$  and integrating in z from -D to 0 yields an equation for  $\psi_n$ . Using (11) and integrating by parts twice gives

$$\psi_{nt} - \beta L_n^2 \psi_{nx} = \frac{f_0 L_n^2 \phi_n(0)}{D} W_E(y) \sin \omega t.$$
 (14)

The surface boundary condition (10) enters through the limits of one of the integration by parts. The value of the vertical mode at the surface is  $\phi_n(0)$ .

The solution to (14), subject to (13), may be written as

$$\psi_n = \frac{4\pi^2 \beta y L_n^2 W_E}{\omega D} \sin(\lambda_n x/2) \cos(\lambda_n x/2 - \omega t) \cos(n\pi z/D) - \frac{\pi^3 h_n' L_n^2 \beta y}{D} \sin(\lambda_n x - \omega t) \cos(n\pi z/D).$$
 (15)

The first term is the variability forced by the Ekman pumping at the surface. This part of the solution is similar in form to the single-layer solution of White (1977) but here the depth-dependent total response is the sum over all modes. It is also similar to the n-mode solution in Spall (2021) but here the Coriolis parameter is allowed to vary with y. This part of the solution consists of a standing wave with wavenumber  $\lambda_n/2$  and zero amplitude on the eastern boundary and a wave that propagates westward at 2 times the long baroclinic Rossby wave speed. The second term represents free waves propagating away from the eastern boundary at the long wave speed due to the fluctuating density anomaly specified through the boundary condition on the layer thickness  $h'_n$  at x = 0.

The time rate of change of the isopycnal surfaces is given by  $(f/N^2)\psi_{zt}$  which, making use of (11), is for each mode

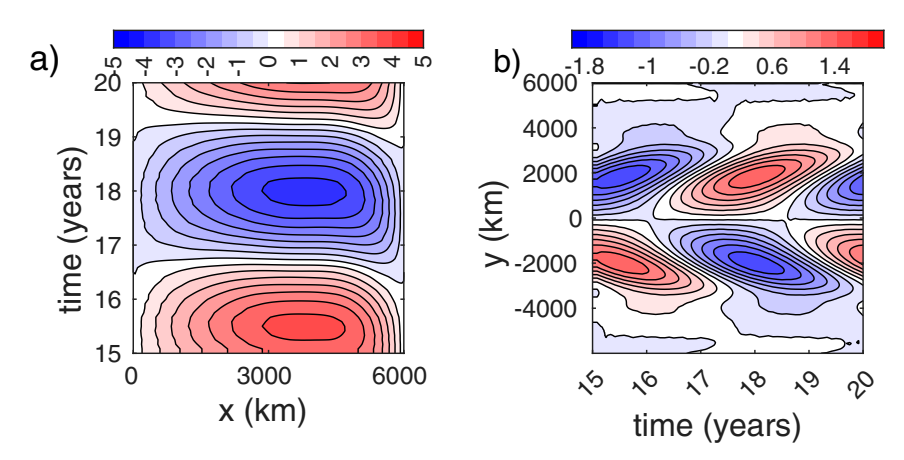


FIG. 5. (a) The zonal overturning circulation (Sv) and (b) the meridional overturning circulation (Sv) for the shallow water model with basin-scale variability in the winds (5) and a 5-yr period.

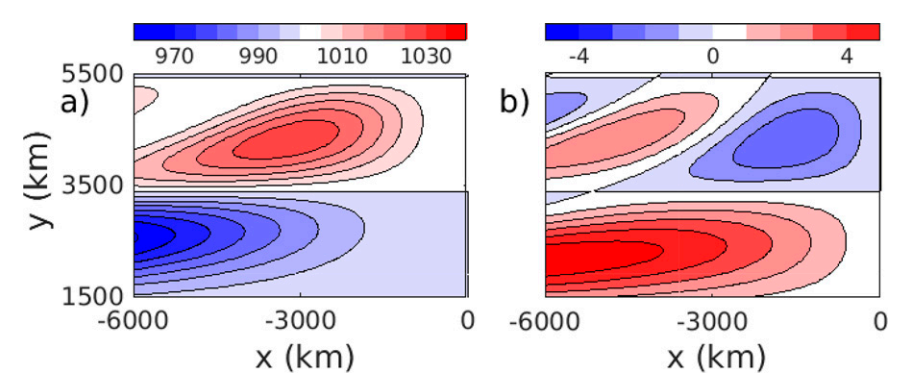


Fig. 6. (a) Upper layer thickness (m) and (b) time rate of change of upper layer thickness  $(10^{-7} \text{ m s}^{-1})$  for the quasigeostrophic theory at the end of the forcing period with the winds (4) and a 10-yr period.

$$h_{nt} = -\frac{4W_E}{\pi} \sin(\lambda_n x/2) \cos(\lambda_n x/2 - \omega t) \sin(n\pi z/D) + h'_n \omega \cos(\lambda_n x - \omega t) \sin(n\pi z/D).$$
 (16)

### a. Zonal overturning circulation

There has been considerable study related to the meridional overturning circulation, as reviewed in section 1, so the focus here is on the zonal overturning circulation. However, the overturning circulation cannot be directly calculated from the quasigeostrophic streamfunction because that represents only the geostrophic part of the flow. Important contributions are also made by ageostrophic terms that are not explicitly represented in the velocity streamfunction. However, since there is no diapycnal mixing in these adiabatic equations, the overturning circulation can be calculated from the integral of the rate of change of the isopycnal interface displacements (Spall 2021). For the ZOC,

$$\Psi_{\text{zoc}}(x) = \sum_{n} \int_{L}^{x} \int_{-L}^{L} h_{nt} dy dx.$$
 (17)

The integral is taken from the southern boundary to the northern boundary and from the eastern boundary westward with an assumption of no normal flow at the eastern boundary. The interface displacement  $h_{nt}$  is provided by (16).

## b. Midlatitude gyre variability

The quasigeostrophic solution is now applied to the problem of variability in the midlatitude gyre winds. For consistency with the shallow water model, and to focus on the dominant signal, only the first baroclinic mode will be considered. The parameters are set to be the same as the example in section 2a with the two-layer shallow water model. The variability in layer thickness on the eastern boundary,  $h'_1$ , was set to zero in this case, consistent with the nearly steady layer thickness found along the eastern boundary of the shallow water model.

The upper layer thickness at zero phase lag (t = nP, where P = 10 years is the forcing period) is shown in Fig. 6a. The

general pattern is similar to that found in the numerical model (Fig. 1a). The subtropical gyre is anomalously thin with a maximum amplitude on the western boundary and zero thickness anomaly on the eastern boundary. The upper layer is anomalously thick in the subpolar gyre with the maximum amplitude found in the central basin. This phase corresponds to the winds transitioning from a negative anomaly to a positive anomaly, so the subtropical and subpolar gyres would both be weaker than average. The dependence of the phase speed on latitude is also evident in the more rapid propagation at lower latitudes.

The time rate of change of the upper layer thickness is shown in Fig. 6b. The subtropical gyre is getting thicker, and the subpolar gyre is getting thinner in the east and thicker in the west. This is consistent with westward phase propagation. Although there are quantitative differences in the amplitude and structure of the upper layer thickness anomalies, they are in broad agreement with what is produced by the shallow water model (Fig. 1b).

The ZOC for this case calculated from (17) is shown in Fig. 7a. The magnitude, westward intensification, and phase shift with longitude all compare well with the overturning diagnosed from the shallow water model (Fig. 2). The main difference is that the phase is shifted such that the theory lags the model by approximately 60°.

## c. Basin-scale variability

The upper layer thickness at zero phase for the basin-scale variability with a 5-yr forcing period is shown in Fig. 8a. The pattern and magnitude of the layer thickness anomalies are close to that found in the shallow water model (Fig. 3a). This calculation used  $h'_1 = 15$  m on the eastern boundary, as found in the shallow water model and expected from Sverdrup theory (discussed in the next section). There is a series of short wavelength waves crossing the basin at high latitudes. At lower latitudes, where the phase speed increases, the wavelength also increases and the contours of constant layer thickness turn westward. Within approximately 2000 km of the equator the layer thickness is essentially uniform. The latitude at which a baroclinic Rossby wave crosses the basin at the forcing period of 5 years is y = 3000 km, so this region of

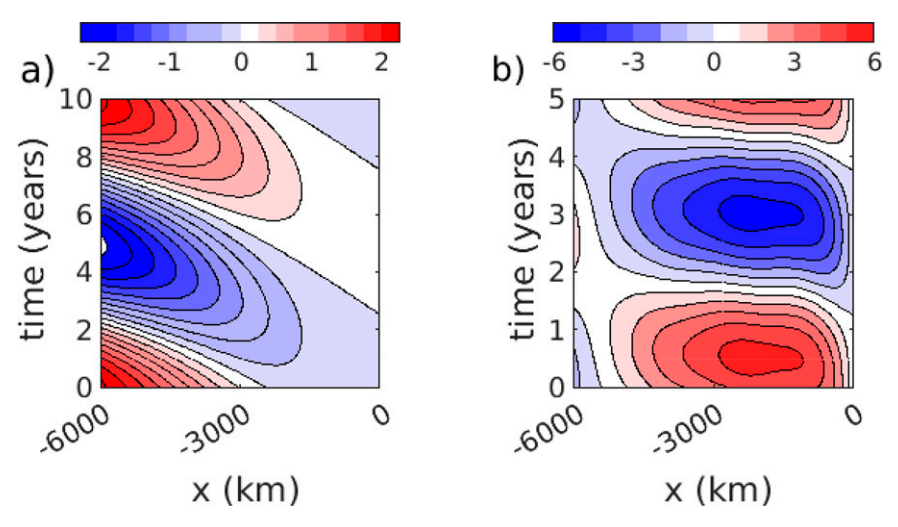


FIG. 7. The zonal overturning circulation from the quasigeostrophic theory for (a) 10-yr period midlatitude gyre and (b) 5-yr period basin-scale variability in winds.

nearly uniform layer thickness is also the region where information from the eastern boundary has fully crossed the basin.

The biggest difference with the numerical model is at high latitudes where the theory produces high wavenumber variability and the numerical model has much weaker variability. This is probably due to dissipation in the model damping the short waves. At y=5000 km, the theoretical wavelength for a 5-yr periodic forcing is approximately  $L_x=2500$  km. The damping rate with a horizontal layer thickness diffusivity of  $500 \text{ m}^2 \text{ s}^{-1}$  is  $L_x^2/(4\pi^2 A_h)=4.5\times 10^8 \text{ s}$ . The phase speed of

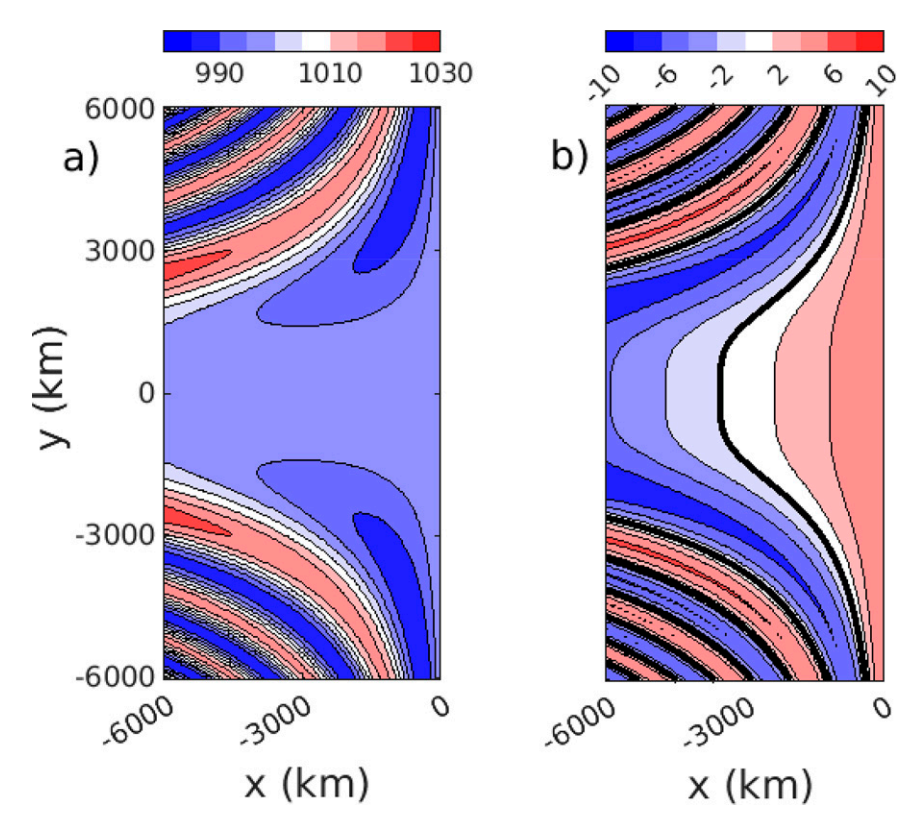


FIG. 8. (a) Upper layer thickness (m) and (b) time rate of change of upper layer thickness  $(10^{-7} \text{ m s}^{-1})$  for the quasigeostrophic theory with midlatitude gyre variability in the winds (5) and a 5-yr period.

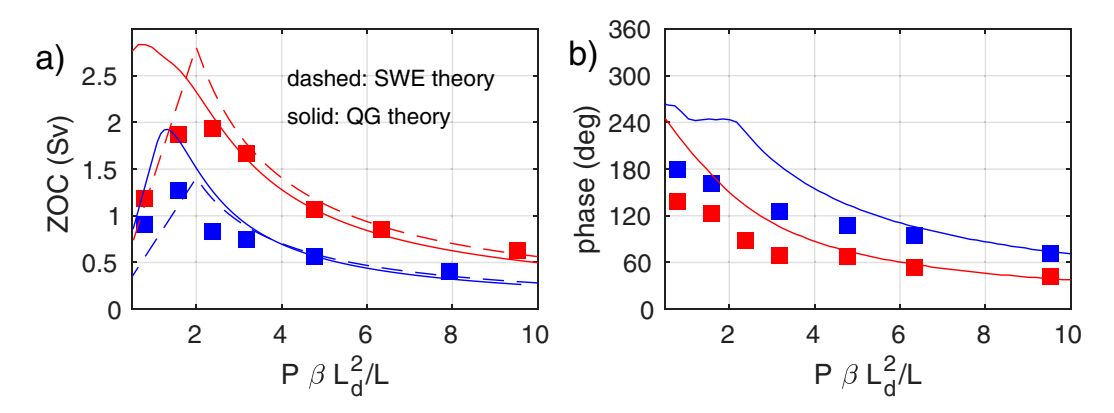


FIG. 9. (a) Amplitude of the zonal overturning circulation as a function of forcing period (scaled by the baroclinic Rossby wave basin-crossing time scale) for  $\beta = 2 \times 10^{-11}$  m<sup>-1</sup> s<sup>-1</sup> (red) and  $\beta = 1 \times 10^{-11}$  m<sup>-1</sup> s<sup>-1</sup> (blue). Squares are for the shallow water model, dashed lines in (a) are from the theory of Spall and Nieves (2020), and the solid lines are from the quasigeostrophic theory.

the first baroclinic mode at that latitude is  $0.015~{\rm m~s^{-1}}$ . It takes  $4\times10^8$  s for this wave to cross the basin, which is very close to the damping time scale. So layer thickness diffusion is likely responsible for the difference between the theory and model at high latitudes.

The time rate of change of the upper layer thickness also compares well with that diagnosed from the shallow water model (Fig. 8b). The layer thickness in the eastern basin is increasing and that in the western basin is decreasing. The phase is nearly independent of latitude within the region near the equator where the layer thickness is uniform. This provides guidance for the development of a simple theoretical estimate of the ZOC in the following section.

### 4. Parameter dependencies

The shallow water model is applied to the two different forcing scenarios with  $\beta=2\times10^{-11}~\text{m}^{-1}~\text{s}^{-1}$  and  $\beta=1\times10^{-11}~\text{m}^{-1}~\text{s}^{-1}$  over a range of forcing frequencies. In each case the basic response is similar to that shown in Figs. 1 and 3. A pattern of wave crests and troughs cross the basin from east to west with longer wavelengths and faster phase speeds at lower latitudes compared to higher latitudes. The purpose of this section is to understand how the frequency of the variability in the winds influences the zonal overturning circulation.

## a. Midlatitude gyre variability

The amplitude of oscillation in the ZOC is shown in Fig. 9 as a function of the forcing period (varied between 1 and 60 years) for both values of  $\beta$ . The forcing period has been scaled by the time it takes a first mode baroclinic Rossby wave to cross the basin at the boundary between the subtropical and subpolar gyres, L/c, where  $c = g'H/\beta y_0^2$  is the baroclinic wave speed and  $H = H_1H_2/(H_1 + H_2)$  is the effective layer thickness. The shallow water model produces a maximum in the ZOC for forcing periods approximately twice the basin-crossing time scale. At this frequency of forcing a free wave would have

the same sign of thickness anomaly all across the basin at the gyre boundary. At longer and shorter periods the amplitude of the ZOC decreases. For very long forcing time scales the ZOC decreases because the system is nearly in equilibrium with the wind. The mass flux required to balance the changing Sverdrup transport is the same, but the transition between inflated and deflated gyre states happens over a longer time period, so the overturning circulation is weaker. At higher frequencies the amplitude decreases because the Ekman pumping changes sign before the basin has had a chance to respond. This midlatitude ZOC is fundamentally connected to the remote MOC, which was discussed by Spall and Nieves (2020). The dashed lines represent the magnitude of the remote MOC as predicted by the heuristic theory of Spall and Nieves (2020), which is given by

$$\Psi_R = \frac{\pi \tau_0 L_g L^2}{2\rho_0 g' H_1} \frac{\min(0.5P/T_{\rm RW}, 1)}{\max(0.5P, T_{\rm RW})}.$$
 (18)

The basin-crossing time scale at the gyre boundary is  $T_{\rm RW} = L/\beta L_d^2$ . The min and max factors account for forcing periods greater and less than  $T_{\rm RW}$  while the coefficient is the maximum value of the remote MOC, which is found for  $P = 2T_{\rm RW}$ .

The agreement between the shallow water model and this theory is reasonably close, demonstrating the connection between the ZOC and the remote MOC. The quasigeostrophic theory developed in section 3 is indicated by the solid lines. The theory compares well with the model at forcing periods longer than the basin-crossing time scale but overpredict the ZOC at higher frequencies. This is especially pronounced for the  $\beta = 2 \times 10^{-11}$  m<sup>-1</sup> s<sup>-1</sup> cases. This may be related to dissipation in the model, which damps the high frequency Rossby waves, particularly at high latitudes.

The phase of the minimum ZOC is shown in Fig. 9b. As was evident for the example at 10-yr forcing period, the phase in the quasigeostrophic theory lags the phase found in the shallow water model. This difference is largest at high

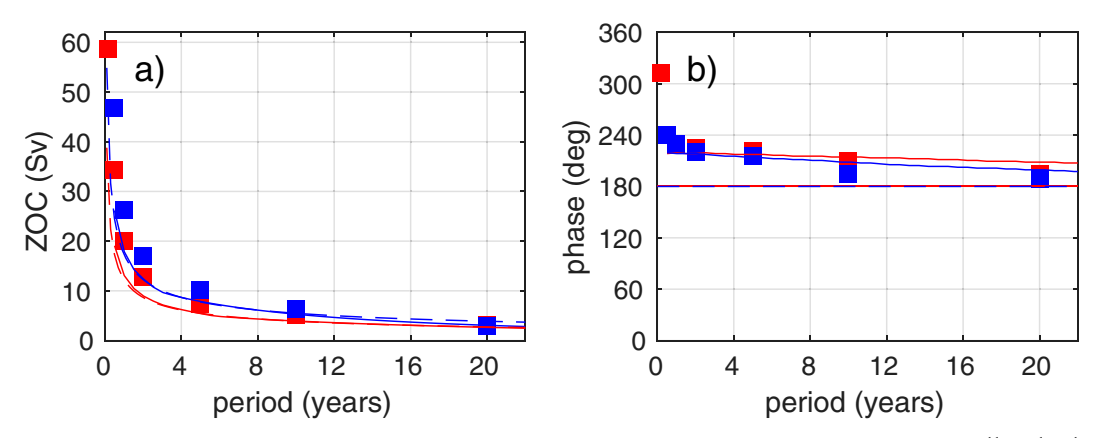


FIG. 10. (a) Amplitude of the zonal overturning circulation as a function of forcing period for  $\beta = 2 \times 10^{-11}$  m<sup>-1</sup> s<sup>-1</sup> (red) and  $\beta = 1 \times 10^{-11}$  m<sup>-1</sup> s<sup>-1</sup> (blue). Squares are for the shallow water model, dashed lines are from the approximate theory (22), and the solid lines are from the quasigeostrophic theory.

frequency and decreases as the forcing period increases. The general trend of decreasing phase with increasing period is found in both the shallow water model and the theory.

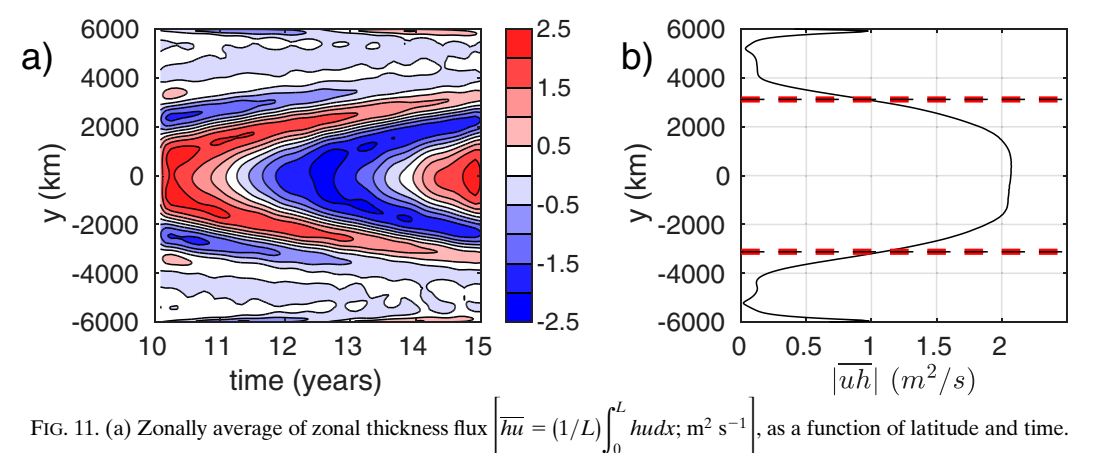
### b. Basin-scale wind variability

The forcing period for the case of variability in the large-scale winds was varied between 0.5 and 20 years. The ZOC diagnosed from the shallow water model increases monotonically as the forcing period decreases (Fig. 10a). For forcing periods less than 1 year the ZOC exceeds 50 Sv. The cases with smaller  $\beta$  produce a stronger ZOC at all forcing periods. The solid lines are the ZOC estimates from the quasigeostrophic theory. Although the theory slightly underpredicts the amplitude of the overturning, the dependence on both frequency and  $\beta$  are both well reproduced. The phase of the minimum ZOC shows only weak dependence on  $\beta$  and forcing period (Fig. 10b). The minimum ZOC, or maximum westward thickness flux, is close to 180° at long periods. This is at the transition between positive wind anomalies and negative

wind anomalies. The zonal mass flux is in phase with the rate of change of the Ekman pumping. This indicates that the forcing period is long compared to the adjustment time scale.

Consideration of the structure of the ZOC allows for construction of a simple analytic estimate of the amplitude of the ZOC as a function of forcing period and the environmental parameters of the system. Figure 11a shows the zonally averaged zonal advection of the upper layer thickness,  $\overline{hu} = (1/L) \int_0^L h_1 u_1 dx$ , as a function of latitude and time. The meridional integral of this quantity is the ZOC. While there is an oscillation at the forcing frequency at all latitudes, the strongest signal is found in the vicinity of the equator. The phase is such that there is an eastward flux of layer thickness when the wind is increasing and a westward flux of layer thickness when the wind is decreasing. This is consistent with the time rate of change of layer thickness at 10 years shown in Fig. 3b. This change in layer thickness is required to

maintain geostrophic balance. The Ekman pumping is uniform



(b) Amplitude of the periodic oscillation in (a) as a function of latitude. The red dashed lines are the latitude at which  $\overline{hu}$  drops to 50% of its maximum value and the black dashed lines are the latitude at which a first mode baroclinic Rossby wave crosses the basin in one forcing period.

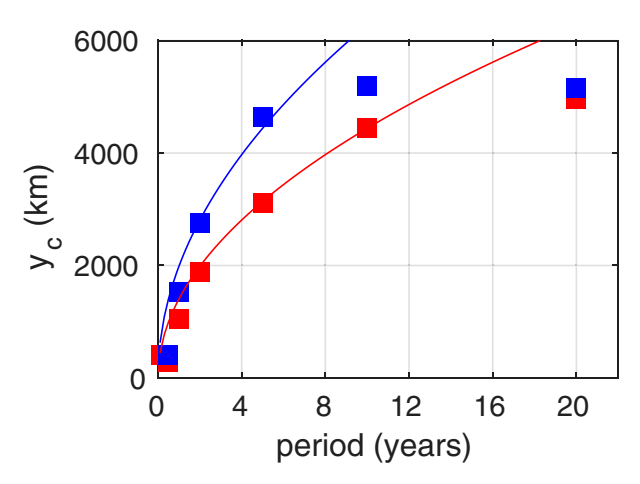


FIG. 12. Squares indicate the latitude at which the average zonal thickness flux drops to 50% of its maximum value as a function of forcing period from the shallow water numerical model. Solid lines indicate the latitude at which the time for a first mode baroclinic Rossby wave to cross the basin matches the forcing period.  $\beta = 2 \times 10^{-11} \, \mathrm{m}^{-1} \, \mathrm{s}^{-1}$  (red) and  $\beta = 1 \times 10^{-11} \, \mathrm{m}^{-1} \, \mathrm{s}^{-1}$  (blue).

at each latitude, upward when the wind stress is positive (years 10–12.5) and downward when it is negative (years 12.5–15). Under Sverdrup balance, the upward Ekman pumping is balanced by the meridional advection of planetary vorticity, so  $v_1 > 0$  and  $\partial h_1/\partial x > 0$ . The deepening in the eastern basin and shoaling in the western basin required to provide this thickness gradient is achieved by the ZOC.

The amplitude of the oscillation in  $\overline{hu}$  as a function of latitude is shown in Fig. 11b. The amplitude is relatively flat near the equator and then decreases nearly linearly to small amplitude at high latitudes. The increase very close to the poleward boundaries is caused by narrow boundary waves and not relevant to the present discussion. The latitude at which the zonal thickness flux decreases to 50% of its maximum value is indicated by the black dashed line. The latitude at which the basin-crossing time scale is equal to the forcing period,  $y_c$ , is indicated by the (nearly coincident) red dashed line:

$$y_c = \left(g'HP/\beta L\right)^{1/2}.\tag{19}$$

This critical latitude is nearly identical to the latitude of 50% reduction in amplitude.

Similar results are found for forcing periods of less than 10 years. A comparison of  $y_c$  with the diagnosed 50% decay latitude is shown in Fig. 12 as a function of forcing period. There is close agreement for  $y_c < L$ , or periods of less than about 10 years. At longer forcing periods  $y_c$  extends beyond the meridional extent of the basin and so cannot be resolved by the model.

The ZOC is predominantly determined by the ocean adjustment required to maintain geostrophic balance under the influence of oscillating winds. Considering the Ekman pumping given by (7), and assuming a steady linear potential vorticity balance, the zonal gradient in the upper layer thickness and the meridional velocity, relative to layer 2, are

$$\frac{\partial h}{\partial x} = \frac{\tau_0 \sin \omega t}{\rho_0 g' H}, \quad v_1 = \frac{\tau_0 \sin \omega t}{\rho_0 \beta y H}.$$
 (20)

Note that the layer thickness is independent of latitude if the flow is in Sverdrup balance. This is important because the ZOC is derived from the time rate of change of the layer thickness and so remains bounded even as the Ekman pumping rate goes to infinity at the equator. Also, the meridional transport has the same magnitude, and opposite sign, from the Ekman transport. Physically, this strong Ekman pumping is balanced by an equally strong meridional velocity and so the mass balance remains finite. The steady assumption is approximately valid for forcing periods for which the first mode baroclinic Rossby wave has crossed the basin, or for  $-y_c < y < y_c$ .

The layer thickness anomaly on the eastern boundary is calculated as  $0.5h_xL$ , or

$$h_e = 0.5\tau_0 L \sin\omega t / \rho_0 g' H_1, \tag{21}$$

and the layer thickness anomaly on the western boundary is  $-h_e$ . For the parameters used here,  $h_e = 15$  m, consistent with the variability produced in the shallow water model (Fig. 4).

As the layer thickness on the eastern boundary increases, the layer thickness at the western boundary decreases and mass is fluxed from west to east. The anomalous volume of upper layer fluid in the eastern basin is  $V=0.25h_eLy_c\sin\omega t$ . The change in volume is provided by the ZOC, with the maximum value located at x=L/2. The maximum ZOC is then given by the time rate of change of the volume of the upper layer in the eastern basin (x>L/2), within the latitude range  $-y_c < y < y_c$ :

$$\Psi_{\text{zoc}} = \frac{\partial V}{\partial t} = \frac{\pi}{2} \frac{\tau_0 L}{\rho_0 g' H} \left( \frac{g' H L}{\beta P} \right)^{1/2} \cos \omega t. \tag{22}$$

This simple analytic estimate is compared to the shallow water model and the quasigeostrophic model in Fig. 10 (dashed lines). The amplitude for both values of  $\beta$  is nearly identical to that predicted by the quasigeostrophic theory. It slightly underpredicts the amplitude at short periods but generally reproduces the dependence on both  $\beta$  and the forcing period. This conceptual model assumes that the ZOC is in quadrature with the winds, so that the minimum ZOC (strongest westward flow) would occurs as the wind anomalies transition from positive to negative, 180° phase.

The magnitude of the ZOC is determined by two competing effects. The first is the zonal gradient in layer thickness, or the thickness anomaly on the eastern boundary. The second is the meridional extent of the quasi-equilibrated region. The ZOC amplitude gets large when the forcing period gets short because the adjustment to geostrophic balance must occur ever more quickly. This is partially offset by the reduction in meridional extent of the region of adjusted flow. However, the region where the flow remains in Sverdrup balance decreases only as  $P^{1/2}$  while the time it takes for the flow to adjust decreases as  $P^{-1}$ , so the strength of the ZOC remains dependent on the forcing period as  $P^{-1/2}$ . The ZOC also

increases as  $L^{3/2}$ . The thickness anomaly on the eastern boundary increases as L, and then the volume anomaly introduces another factor of L through the zonal integral. These increases are partially offset by the decrease in critical latitude as  $L^{-1/2}$ , resulting in the 3/2 dependence. The combination g'H reduces the layer thickness gradient, but it increases the baroclinic wave speed (and thus  $y_c$ ), with the net result being a  $(g'H)^{1/2}$  dependence. The  $\beta$  is involved only through its influence on the long baroclinic Rossby wave speed and  $y_c$ .

The estimate (22) for the ZOC is identical to the Sverdrup transport at latitude  $y_c$ . Also recall that the Sverdrup transport is of equal magnitude and opposite sign to the Ekman transport. So one can think of the ZOC as a large  $\beta$  plume (Stommel 1982) forced by the Ekman pumping. Positive wind stress anomalies drive an eastward zonal flow which turns to the north and flows to higher latitudes while the Ekman pumping causes the upper layer thickness to increase. It is also similar (except for a factor of  $\pi$ ) to the geostrophic flow forced by a layer thickness change of  $h_e$  at latitude  $y_c$ , so the zonal flow is supported by the meridional layer thickness gradient that results from the difference in the zonal phase speed with latitude.

### 5. Discussion and conclusions

The variability in the ZOC forced by winds can be as large or larger than that of the MOC. This is not surprising since the overturning circulation is three dimensional. Nonetheless, the ZOC has received much less consideration than the MOC, both in terms of description and theory. The present study outlines how the ZOC arises as a result of the timedependent adjustment toward a geostrophic balance under forcing by transient winds. At midlatitudes the largest response is found for forcing periods close to the basin-crossing time scale for baroclinic Rossby waves. The ZOC acts to provide the mass flux into or out of the subpolar gyre that cannot be supplied by the subtropical gyre. This transport is communicated from lower latitudes in western boundary currents, thus the ZOC acts to exchange water between the boundary and the interior. At low latitudes the magnitude of the ZOC increases with increasing frequency of wind variability. In these cases the ZOC can greatly exceed the MOC as water sloshes back and forth from the western to eastern basin; however, the exchange between the western boundary and the interior is weak.

The dynamics of the ZOC are fundamentally different from that of the MOC. A dominant component of the MOC is the geostrophic flow, both in the western boundary currents and in the gyre interior (Frajka-Williams et al. 2016). The geostrophic component of the MOC variability is generally in the opposite direction to the Ekman transport. The net meridional geostrophic flow at each latitude depends on the change in pressure between the eastern and western boundaries (Johnson et al. 2019). However, for meridionally confined wind stress anomalies, there is no change in pressure in the meridional direction from one side of the anomalous wind to the other. Yet the results presented here show that there can still be significant net zonal flow, as large or larger than the

variability in the MOC. This is because the geostrophic transport depends not only on the change in pressure but also on the Coriolis parameter. For the MOC the Coriolis parameter is constant with longitude at each latitude. For the ZOC the Coriolis parameter varies with latitude at each longitude. This results in a net zonal flow because, while the total pressure change is zero across each latitude section, the pressure gradients occur at different latitudes. For the cases studied here, the ZOC is perpendicular to the Ekman transport and thus does not contain a contribution from the barotropic mode identified by Bryan (1982) and Jayne and Marotzke (2001).

Because of its baroclinic structure, the ZOC results in a net zonal transport of heat and other tracers. The relationship between the zonal heat flux and the ZOC, for a two-layer fluid, is simply

$$ZHF = \rho_0 C_p \Delta T \Psi_{zoc}, \qquad (23)$$

where  $\rho_0$  is a reference density,  $C_p$  is the specific heat of seawater, and  $\Delta T$  is the change in temperature between the upper and lower layers. For the examples presented here  $g'=0.01~{\rm m~s^{-2}}$  and, taking a representative value for the thermal expansion coefficient of  $\alpha=0.15~C^{-1}$ , gives  $\Delta T=6.7^{\circ}{\rm C}$ . Each Sverdrup of zonal mass transport then carries a zonal heat flux of 27 TW. This scales linearly with stratification, so larger  $\Delta T$  would result in larger heat flux; however, changes in  $\Delta T$  will result in changes in the ZOC.

For the midlatitude wind variability, Spall and Nieves (2020) found that the ZOC scales as  $g'^{-1}$  [Eq. (18)], so the ZHF is, somewhat surprisingly, independent of stratification if the change in density between the two layers is proportional to  $\Delta T$ . In the limit of very weak stratification the interface displacements required for Sverdrup balance, and thus the ZOC, increase, which offsets the decrease in the ZHF per unit of transport. This will also, however, shift the forcing for which the solution attains the maximum heat transport to longer periods. Using (18), the maximum ZHF for the midlatitude winds is

$$ZHF_{mid} = \frac{\pi \rho_0 C_p \tau_0 L_g L^2}{gH_1 \alpha P}$$
 (24)

and is found for  $P = 2T_{RW}$ .

The ZOC for the low-latitude, large-scale wind variability scales as  $g'^{-1/2}$  [Eq. (22)] so that the ZHF increases as  $g'^{1/2}$ :

$$ZHF_{low} = \frac{\pi C_p \tau_0 L}{2g\alpha H_1} \left(\frac{g'HL}{\beta P}\right)^{1/2}.$$
 (25)

This dependence on stratification remains because both the adjustment time scale and the latitude range over which the adjustment takes place vary with stratification.

A midlatitude ZOC of 2 Sv would produce a zonal heat flux of O(50) TW. This is comparable to the interannual meridional heat flux variability due to both large-scale processes and mesoscale eddies at midlatitudes (Roemmich and Gilson 2001; Volkov et al. 2008; Zhao et al. 2018). However, the wind-driven ZOC at low latitudes can exceed 20 Sv, producing zonal heat flux variability of O(0.5) PW. This is also

comparable to observed and simulated variability in the meridional heat flux at low latitudes (Volkov et al. 2008; Tandon et al. 2020). Although the ZOC and related zonal heat flux have not received as much attention as their meridional counterparts, they have comparable magnitudes for interannual variability, which suggests a dynamic role for the ZOC in the context of air–sea exchange and atmospheric interannual variability, especially so at low latitudes.

Acknowledgments. This study was supported by National Science Foundation Grants OCE-1947290 and OCE-2122633. Helpful suggestions from two anonymous reviewers helped to improve the presentation.

### REFERENCES

- Abraham, J. P., and Coauthors, 2013: A review of global ocean temperature observations: Implications for ocean heat content estimate and climate change. *Rev. Geophys.*, 51, 450– 483, https://doi.org/10.1002/rog.20022.
- Anderson, D. L. T., and A. Gill, 1975: Spin-up of a stratified ocean with application to upwelling. *Deep-Sea Res.*, **22**, 583–596, https://doi.org/10.1016/0011-7471(75)90046-7.
- Bell, M. J., A. T. Blaker, and J. J.-M. Hirschi, 2021: Wind-driven oscillations in the meridional overturning circulation near the equator. Part II: Idealized simulations. *J. Phys. Oceanogr.*, 51, 662–683, https://doi.org/10.1175/JPO-D-19-0297.1.
- Biastoch, A., C. W. Böning, J. Getzlaff, J. M. Molines, and G. Madec, 2008: Causes of interannual-decadal variability in the meridional overturning circulation of the midlatitude North Atlantic Ocean. J. Climate, 21, 6599–6615, https://doi. org/10.1175/2008JCL12404.1.
- Blaker, A. T., J. J.-M. Hirschi, M. J. Bell, and A. Bokota, 2021: Wind-driven oscillations in the meridional overturning circulation near the equator. Part I: Numerical models. *J. Phys. Oceanogr.*, 51, 645–661, https://doi.org/10.1175/JPO-D-19-0296.1.
- Bryan, K., 1982: Seasonal variation in meridional overturning and poleward heat transport in the Atlantic and Pacific Oceans. *J. Mar. Res.*, **40**, 39–53.
- Cessi, P., and P. Otheguy, 2003: Oceanic teleconnections: Remote response to decadal wind forcing. J. Phys. Oceanogr., 33, 1604–1617, https://doi.org/10.1175/2400.1.
- —, K. Bryan, and R. Zhang, 2004: Global seiching of thermocline waters between the Atlantic and the Indian-Pacific Ocean Basins. *Geophys. Res. Lett.*, 31, L04302, https://doi.org/ 10.1029/2003GL019091.
- Evans, D. G., J. Toole, G. Forget, J. D. Zika, A. C. N. Garabato, A. J. Nurser, and L. Yu, 2017: Recent wind-driven variability in Atlantic water mass distribution and meridional overturning circulation. *J. Phys. Oceanogr.*, 47, 633–647, https://doi. org/10.1175/JPO-D-16-0089.1.
- Frajka-Williams, E., and Coauthors, 2016: Compensation between meridional flow components of the Atlantic MOC at 26 N. *Ocean Sci.*, 12, 481–493, https://doi.org/10.5194/os-12-481-2016.
- Grist, J. P., and Coauthors, 2010: The roles of surface heat flux and ocean heat transport convergence in determining Atlantic Ocean temperature variability. *J. Phys. Oceanogr.*, **60**, 771–790, https://doi.org/10.1007/s10236-010-0292-4.

- Häkkinen, S., P. B. Rhines, and D. L. Worthen, 2015: Heat content variability in the North Atlantic Ocean in reanalysis. Geophys. Res. Lett., 42, 2901–2909, https://doi.org/10.1002/2015GL063299.
- Huang, R. X., 2015: Heaving modes in the world oceans. *Climate Dyn.*, 45, 3563–3591, https://doi.org/10.1007/s00382-015-2557-6.
- Jayne, S. R., and J. Marotzke, 2001: The dynamics of ocean heat transport variability. Rev. Geophys., 39, 385–411, https://doi. org/10.1029/2000RG000084.
- Johnson, H. L., and D. P. Marshall, 2004: Global teleconnections of meridional overturning circulation anomalies. *J. Phys. Oceanogr.*, **34**, 1702–1722, https://doi.org/10.1175/1520-0485 (2004)034<1702:GTOMOC>2.0.CO;2.
- —, P. Cessi, D. P. Marshall, F. Schloesser, and M. A. Spall, 2019: Recent contributions of theory to our understanding of the Atlantic meridional overturning circulation. *J. Geo*phys. Res. Oceans, 124, 5376–5399, https://doi.org/10.1029/ 2019JC015330.
- Kanzow, T., and Coauthors, 2010: Seasonal variability of the Atlantic meridional overturning circulation at 26.5°N. J. Climate, 23, 5678–5698, https://doi.org/10.1175/2010JCLI3389.1.
- Kawase, M., 1987: Establishment of deep ocean circulation driven by deep-water production. J. Phys. Oceanogr., 17, 2294–2317, https://doi.org/10.1175/1520-0485(1987)017<2294:EODOCD>2. 0.CO;2.
- LaCasce, J. H., 2000: Baroclinic Rossby waves in a square basin.
  J. Phys. Oceanogr., 30, 3161–3178, https://doi.org/10.1175/1520-0485(2000)030<3161:BRWIAS>2.0.CO;2.
- Levitus, S., and Coauthors, 2012: World ocean heat content and thermosteric sea level change (0–2000 m), 1955–2010. *Geophys. Res. Lett.*, **39**, L10603, https://doi.org/10.1029/2012GL051106.
- Lozier, M. S., S. Leadbetter, R. G. Williams, V. Roussenov, M. S. C. Reed, and N. J. Moore, 2008: The spatial pattern and mechanisms of heat-content change in the North Atlantic. *Science*, 319, 800–803, https://doi.org/10.1126/science.1146436.
- McCarthy, G. D., and Coauthors, 2015: Measuring the Atlantic meridional overturning circulation at 26.5°N. *Prog. Ocean-ogr.*, 130, 91–111, https://doi.org/10.1016/j.pocean.2014.10.006.
- Pillar, H., P. Heimbach, H. Johnson, and D. Marshall, 2016: Dynamical attribution of recent variability in Atlantic overturning. J. Climate, 29, 3339–3352, https://doi.org/10.1175/ JCLI-D-15-0727.1.
- Polo, I., J. Robson, R. Sutton, and M. A. Balmaseda, 2014: The importance of wind and buoyancy forcing for the boundary density variations and the geostrophic component of the AMOC at 26°N. J. Phys. Oceanogr., 44, 2387–2408, https:// doi.org/10.1175/JPO-D-13-0264.1.
- Roemmich, D., and C. Wunsch, 1985: Two transatlantic sections: Meridional circulation and heat flux in the subtropical North Atlantic Ocean. *Deep-Sea Res.*, 32, 619–664, https://doi.org/ 10.1016/0198-0149(85)90070-6.
- —, and J. Gilson, 2001: Eddy transport of heat and thermocline Waters in the North Pacific: A key to interannual/decadal climate variability? *J. Phys. Oceanogr.*, 31, 675–687, https://doi. org/10.1175/1520-0485(2001)031<0675:ETOHAT>2.0.CO;2.
- Spall, M. A., 2021: An idealized modeling study of the midlatitude variability of the wind-driven meridional overturning circulation. J. Phys. Oceanogr., 51, 2425–2441, https://doi.org/10. 1175/JPO-D-20-0317.1.
- —, and D. Nieves, 2020: Wind-forced variability of the remote overturning circulation. *J. Phys. Oceanogr.*, **50**, 455–469, https://doi.org/10.1175/JPO-D-19-0190.1.

- Stommel, H., 1982: Is the South Pacific helium-3 plume dynamically active? *Earth Planet. Sci. Lett.*, 61, 63–67, https://doi.org/10.1016/0012-821X(82)90038-3.
- Sturges, W., and B. G. Hong, 1995: Wind forcing of the Atlantic thermocline along 32°N at low frequencies. *J. Phys. Oceanogr.*, **25**, 1706–1715, https://doi.org/10.1175/1520-0485(1995)025 <1706:WFOTAT>2.0.CO;2.
- Tandon, N. F., O. A. Saenko, M. A. Kane, and P. J. Kushner, 2020: Interannual variability of the global meridional overturning dominated by the Pacific variability. *J. Phys. Oceanogr.*, 50, 559–574, https://doi.org/10.1175/JPO-D-19-0129.1.
- Volkov, D. L., T. Lee, and L.-L. Fu, 2008: Eddy-induced meridional heat transport in the ocean. *Geophys. Res. Lett.*, 35, L20601, https://doi.org/10.1029/2008GL035490.
- Wei, T., R. X. Huang, W. Wang, and X. Wang, 2015: Zonal overturning circulation and heat flux induced by heaving modes in the world oceans. *Acta Oceanol. Sin.*, 34, 80–91, https://doi. org/10.1007/s13131-015-0751-3.
- White, W. B., 1977: Annual forcing of baroclinic long waves in the tropical North Pacific Ocean. J. Phys. Oceanogr., 7, 50–61, https://doi.org/10.1175/1520-0485(1977)007<0050: AFOBLW>2.0.CO;2.
- Williams, R. G., V. Roussenov, D. Smith, and M. S. Lozier, 2014: Decadal evolution of ocean thermal anomalies in the North Atlantic: The effects of Ekman, overturning, and horizontal transport. J. Climate, 27, 698–719, https://doi.org/10.1175/ JCLI-D-12-00234.1.

- Yang, J., 2015: Local and remote wind-stress forcing of the seasonal variability of the Atlantic Meridional Overturning Circulation (AMOC) transport at 26.5°N. J. Geophys. Res. Oceans, 120, 2488–2503, https://doi.org/10.1002/2014JC010317.
- Yeager, S., and G. Danabasoglu, 2014: The origins of late twentieth-century variations in the large-scale North Atlantic circulation. J. Climate, 27, 3222–3247, https://doi.org/10.1175/JCLI-D-13-00125.1.
- Zhao, J., and W. Johns, 2014a: Wind-driven seasonal cycle of the Atlantic meridional overturning circulation. *J. Phys. Oceanogr.*, 44, 1541–1562, https://doi.org/10.1175/JPO-D-13-0144.1.
- —, and —, 2014b: Wind-forced interannual variability of the Atlantic meridional overturning circulation at 26.5°N. J. Geophys. Res. Oceans, 119, 2403–2419, https://doi.org/10. 1002/2013JC009407.
- —, A. Bower, J. Yang, X. Lin, and N. P. Holliday, 2018: Meridional heat transport variability induced by mesoscale processes in the subpolar North Atlantic. *Nat. Commun.*, 9, 1124, https://doi.org/10.1038/s41467-018-03134-x.
- Zou, S., M. S. Lozier, and M. Buckley, 2019: How is meridional coherence maintained in the lower limb of the Atlantic meridional overturning circulation? *Geophys. Res. Lett.*, 46, 244–252, https://doi.org/10.1029/2018GL080958.
- —, and X. Xu, 2020: Latitudinal structure of the meridional overturning circulation variability on interannual to decadal time scales in the North Atlantic Ocean. *J. Climate*, 33, 3845–3862, https://doi.org/10.1175/JCLI-D-19-0215.1.